Electronic Supplement 5

The dual-band method: A history of its application to volcanic hot spots

Until 2005 around half (48 %) of the work achieved in the sphere of satellite-based volcano radiometry had focused on quantifying the sub-pixel thermal structure of volcanic hot spots. As can been seen from Figure A1 of Appendix A, the importance of this work did not diminish through time, being the dominant theme area each year between 1989 and 2001. This is a measure of the importance ascribed to quantifying volcanic heat fluxes using IR data which, of course, is its natural role.

Efforts to extract thermal surface structures from IR pixels have been based on the mixture models explored in Chapter 4. These models have been heavily influenced by a methodology commonly known as the *dual-band technique* or the *dual-band method*. The method was introduced by Dozier (1980) in a *NOAA technical memorandum* of 1980, and in a subsequent paper published in *Remote Sensing of Environment* (Dozier, 1981). The method allows estimation of the size and temperature of a sub-pixel hot spot using two bands of IR data. To achieve this, Dozier (1981) recommended using unsaturated data acquired in AVHRR channels 3 and 4, and solving the simultaneous equations (Equations 4.8) of Chapter 4 by assuming a background temperature from non-anomalous pixels surrounding the target pixel. This was the method subsequently applied by Matson and Dozier (1981) to estimate the size and temperature of sub-pixel hot spots apparent in AVHRR data due to steel mills and oil field gas flares. Between the publication of these landmark papers and 2005, a total of 43 papers dealt with the subject of pixel mixture modeling over volcanic hot spots or application of the dual-band method, this being theme 2 of the literature collation given in Table A2 of Appendix A. Although initially designed by Dozier (1980; 1981) to work with AVHRR data, applications to TM and ETM+ data have led the way in volcanology, with 30 of the 43 papers published in this theme area between 1980 and 2005 focusing on application of the dual band method to TM and ETM+ data.

Application of the dual-band method to TM-class data

Application and modification of the dual-band method was the foundation of much of the early hot spot applications of TM data in volcanology. Following the pivotal papers of

Francis and Rothery (1987) and Rothery *et al.* (1988) (see Chapter 1), the community was quick to pick up on the ability of the dual-band method to extract sub-pixel thermal structures from TM-class data, with progress up until 2000 being summarized in Table S5.1. Table S5.1 shows that application of the dual-band method, and modification to suit different data limits and hot spot types, was fully evolved by 2000. By 2000, applications were thus increasingly based on already-developed methodologies, selecting a solution model depending on the limits of the data, the feature type present in the pixel and the assumptions that could be made.

Rothery et al. (1988)

Francis and Rothery (1987) pointed to the differences (by 50 °C to 100 °C) between temperatures derived from Landsat bands 5 and 7 for pixels over Lascar's active lava dome, suggesting that the hot source may be thermally inhomogeneous over a spatial scale that was smaller than the pixel dimension. However, although this difference is the basis of the dual-band methodology (see Section 4.1.1.3 of Chapter 4), they did not apply the dual-band method. Rothery *et al.* (1988) was the first to actually apply the dual-band method to estimate the sub-pixel thermal structure over an active volcanic source. They assumed that a single radiant source occupied part of an otherwise non-radiant pixel to calculate the size and temperature of the radiant source from unsaturated DNs in Landsat bands 5 and 7. In other words, they applied the unique one-component solution of Section 4.2.1.2 of Chapter 4, a solution which relies on only one thermal source contributing to the pixel-integrated radiance. The resulting solution curves of Rothery *et al.* (1988) are reproduced here in Figure S5.1 and show the classic graphical dual-band solution. For such a solution, size and temperature combinations of the sub-pixel hot spot that provide a given DN (or radiance) in the two bands are plotted, and solution occurs where the two curves cross.

Pieri et al. (1990)

Although the approach of Rothery *et al.* (1988) was subsequently applied to TM data for active lava lakes and domes by Glaze *et al.* (1989), it was Pieri *et al.* (1990) who applied the dual-band method in its true two component form over an active lava. To do this, they used a TM scene of lava active at Mount Etna, assumed a crust temperature (of 125 °C) and used unsaturated data in bands 5 and 7 to estimate the size and temperature of the hot cracks present in the lava flow. For pixels saturated in band 7, crust temperature was set to the band 7 saturation temperatures, and to the band 5 saturation temperature if both bands 5 and 7 were saturated. The same approach and assumptions were applied in a paper published the following year by Abrams *et al.* (1991) to estimate the thermal structure for hot spots at Fuego and Colima volcanoes (see Table S5.1).

Table S5.1. *Application and development of the dual-band method to satellite data containing volcanic hot spots, 1980–2000. For each case we give (i) the sensor, spectral regions and bands used, (ii) the method applied (as defined in Chapter 4), (iii) and heat/mass flux parameters calculated using dual-band results, including radiative, convection and conductive heat fluxes (M_{rad}, M_{conv} and M_{cond}), as well as time-averaged discharge rates (TADR). T_c = crust temperature, T_n = hot crack temperature, T_b = ambient background temperature and P_b = pixel portion occupied by cold background. For band definitions and waveband ranges see Appendices C (for TM) and D (for AVHRR and ATSR)*

Reference	Sensor	Spectral Region	Bands	Method (Section in Chapter 4)	Assumptions	M_{rad}	M_{conv}	M_{cond}	TADR	Other
Rothery *et al.* (1988)	TM	SWIR	5,7	One-radiant-component, two SWIR bands (4.2.1.2)	None	–	–	–	–	–
Glaze *et al.* (1989)	TM	SWIR	5,7	One-radiant-component, two SWIR bands (4.2.1.2)	None	✓	–	–	–	–
Pieri *et al.* (1990)	TM	SWIR	5,7	Dual-Band (4.2.1.1)	T_c	✓	–	–	–	(A)
Abrams *et al.* (1991)	TM	SWIR	5,7	Dual-Band (4.2.1.1)	T_c	✓	–	–	–	–
Oppenheimer (1991)	TM	SWIR	5,7	Dual-Band (4.2.1.1)	T_h	✓	✓	–	–	(B)
Oppenheimer (1991)	TM	TIR	6	Two-component, one TIR band (4.2.1.4)	T_c,T_b	–	–	–	–	(C)
Bhattacharya *et al.* (1993)	TM	SWIR	5,7	Dual-Band (4.2.1.1)	T_c	–	–	–	–	–
Gupta & Badarinath (1993)	TM	SWIR	5,7	Two-component, one SWIR band (4.2.1.4)	None	–	–	–	–	(D)
Oppenheimer (1993a)	TMS	SWIR, TIR	9,10,11	Three bands, three-components two assumptions (4.3.1.1)	T_h,T_b	–	–	–	–	–
Oppenheimer *et al.* (1993)	TM	SWIR	5,7	Dual-Band (4.2.1.1)	T_h	–	–	–	–	–

Table S5.1. (*cont.*)

Reference	Sensor	Spectral Region	Bands	Method (Section in Chapter 4)	Assumptions	M_{rad}	M_{conv}	M_{cond}	TADR	Other
Reddy *et al.* (1993)	TM	SWIR	5,7	Dual-Band (4.2.1.1)	T_c	–	–	–	–	–
Flynn *et al.* (1994)	TM	SWIR	5,7	Dual-Band (4.2.1.1)	T_h	✓	–	–	–	–
Flynn *et al.* (1994)	TM	TIR	6	Two-component, one TIR band (4.4.1.7)	T_h,T_b	✓	–	–	–	(E)
Andres & Rose (1995)	TM	NIR, SWIR	4,5	One-radiant-component, two SWIR bands (4.2.1.2)	None	–	–	–	–	–
Harris *et al.* (1997a)	AVHRR	TIR	4	Two-component, one TIR band (4.3.1.2)	T_c,T_b	✓	✓	✓	✓	–
Harris *et al.* (1997b)	AVHRR	TIR	4	Two-component, one TIR band (4.3.1.2)	T_c,T_b	✓	✓	✓	✓	–
Oppenheimer & Francis (1997)	TM	NIR, SWIR	4,5,7	Dual-Band + constraint from non-response (or response) in the NIR (4.3.1.4)	T_h	✓	✓	–	–	–
Wooster & Rothery (1997a)	ATSR	TIR	11 μm	Two-component, one TIR band (4.3.1.2)	T_c,T_b	–	–	–	–	–
Wooster & Rothery (1997b)	ATSR	TIR	11 μm	Two-component, one TIR band (4.3.1.2)	T_c,T_b	–	–	–	–	–
Wooster *et al.* (1997)	ATSR	TIR	11 μm	Two-component, one TIR band (4.3.1.2)	T_c,T_b	✓	✓	✓	–	–
Harris *et al.* (1998)	TM	SWIR	5,7	Dual-Band* (4.2.1.1)	T_h	✓	✓	✓	✓	(F)

Harris *et al.* (1998)	AVHRR	TIR	4	Two-component, one TIR band (4.3.1.2)	T_c,T_b	✓	✓	✓	✓	(F)
Oppenheimer (1998)	TM	SWIR	5,7	One-radiant-component SWIR + multiple pixel integration (4.2.1.2 + 4.3.1.3)	None	✓	–	–	–	–
Harris *et al.* (1999a)	TM	NIR, SWIR	4,5,7	Three component, one band + constraint from non-responsive and saturated bands (4.3.1.1 + 4.3.1.4)	T_h, p_b, T_b	✓	✓	–	✓	–
Harris *et al.* *emphasis>* *(1999a)*	TM	SWIR, TIR	5,7,6	Three-component, three bands Mixed Spatial Resolutions (4.3.1.1 + 4.3.1.3)	T_h	✓	✓	–	✓	–
Harris *et al.* (1999b)	AVHRR	TIR	4	Two-component, one TIR band (4.3.1.2)	T_c,T_b	✓	✓	–	✓	–

* These were essentially the dual-band results of Flynn *et al.* (1994) [same method, same data, same IDL software], but applied to develop a more complete heat flux model for the entire tube-fed lava flow system (see note F).

(A) = Core cooling rate

(B) = Surface crust thickness

(C) = Lava flow width

(D) = Vent area/temperature combinations

(E) = Skylight area

(F) = Heat flux models for surface lava flows, tube-contained flow and ocean-entry flow applied

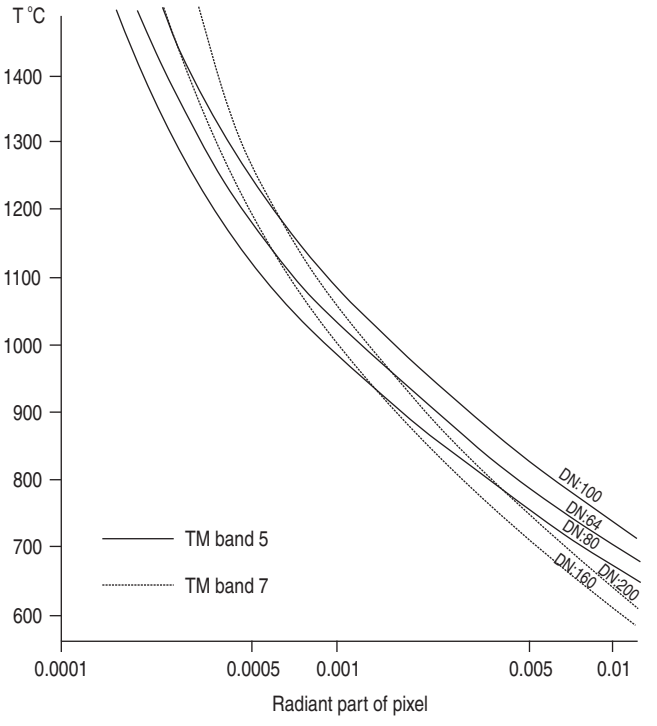

Figure S5.1 "Surface temperature of a radiant area occupying part of an otherwise nonradiant pixel, and the size of that area expressed as a proportion of a pixel, calculated from selected radiant DN in Landsat TM bands 5 and 7. The solution for temperature and area when DN is measured in two bands is given by the crossover between the appropriate curves for the DN in each band. For example, if the radiant DN in band 5 is 100 and that in band 7 is 200, then the derived surface temperature is 1200 °C emanating from about 0.0006 of a pixel" – Original figure caption wording of Rothery *et al.* (1988) From Rothery *et al.* (1988, Fig. 2): Reproduced by permission of American Geophysical Union.

Oppenheimer (1991)

While Oppenheimer (1991) applied the dual-band method to TM data for the 1989 lava flow of Lonquimay (Chile), Oppenheimer *et al.* (1993) applied it to TM data for Lascar's active lava dome. Like Pieri and Baloga (1990), both studies used TM bands 5 and 7 data to solve the dual-band method in its two-component form over an active lava, but instead chose to assume the (slightly easier to set) hot component (crack) temperature to solve for the lava crust temperature and area. Like Pieri *et al.* (1990), Oppenheimer (1991) also took into account problems of saturation and non-response:

- In cases where band 7 was saturated, solution was achieved using the saturated band 7 radiance with the unsaturated band 5 radiance; the output crust temperature was assumed to equate to the lower limit for the true value (that is, the band 7 pixel-integrated temperature was probably higher, so that a higher crust temperature would be required for actual solution).

- If band 5 was non-responsive, the band 7 pixel-integrated temperature was used as an upper limit for the likely crust temperature (that is, hot cracks were probably present, so a lower crust temperature was probably required to balance the integrated band 7 radiance).

Oppenheimer's (1991) results for Lonquimay's 1989 lava flow are plotted as a function of down-flow distance in Figure 4.11b of Chapter 4.

Oppenheimer (1991) was also the first to apply the two-component TIR solution of Section 4.3.1.2 (Chapter 4). Following this method, Oppenheimer (1991) assumed that the area occupied by hot cracks in the active lava was trivial so that the radiant contribution of this high temperature component was negligible in TM's TIR band (band 6). This meant that the pixel fraction occupied by crusted lava (*f*) could be estimated from:

$$f = (R_6 - R_0) / (R_s - R_0)$$

R_6 being the pixel-integrated radiance in band 6 (corrected for emissivity and atmospheric effects), R_0 being the radiance from ambient surfaces within the pixel and surrounding the lava flow (obtained from pixels surrounding the hot spot pixel), and R_s being the radiance from a crusted lava surface for each pixel (as assumed from the bands 5 and 7 dual-band results). Next the lava area (A_{lava}) within each 120 m band 6 pixel was estimated by multiplying *f* by the pixel area (A_{pixel}), where Oppenheimer (1991) obtained a range of:

$$A_{lava} = f\ A_{pixel} = 0.13 \text{ x } 14\,400\ m^2 = 1870\ m^2$$

to

$$A_{lava} = f\ A_{pixel} = 0.25 \text{ x } 14\,400\ m^2 = 3600\ m^2$$

Assuming that the flow was orientated at right-angles to the pixel, Oppenheimer (1991) used these calculations to estimate flow width (W_{flow}) by dividing by pixel length (L_{pixel}), to obtain widths of:

$$W_{flow} = A_{lava} / L_{pixel} = 1870\ m^2 / 120\ m = 16\ m$$

to

$$W_{flow} = A_{lava} / L_{pixel} = 3600\ m^2 / 120\ m = 30\ m$$

Further applications and modifications through the 1990s

Throughout the 1990s a series of studies further modified and adapted the dual-band method to satellite data containing volcanic hot spots.

(1) The Barren Island publication series

Three papers published in 1993 considered application of the dual-band method to TM data containing active basaltic lava flows and open vents at Barren Island (Bhattacharya *et al.*, 1993; Gupta and Badarinath, 1993; Reddy *et al.*, 1993). Both Bhattacharya *et al.* (1993) and

Reddy *et al.* (1993) followed the method of Pieri *et al.* (1990), assuming a crust temperature (200 °C) and solving for the temperature and area of hot cracks. While Bhattacharya *et al.* (1993) applied the method to six daytime TM images acquired between 3 March and 22 May 1991, Reddy *et al.* (1993) considered a nighttime image acquired on 8 July 1991.

At the same time Gupta and Badarinath (1993) considered TM data from the 6 May 1991 acquired over the assumed location of an active vent. Both bands 5 and 7 were saturated, but band 4 was responsive, the DN (35) converted to a pixel-integrated brightness temperature of 1084 K which, when corrected for reflection and emissivity effects, was reduced to 1015 K. Gupta and Badarinath (1993) then used a two component model (hot vent against cold background) to estimate the range of vent sizes and temperatures that could account for the band 4 pixel-integrated temperature given an assumed background radiance. This is solution option (1) of Section 4.2.1.4. of Chapter 4.

(2) Flynn et al. (1994)

Flynn *et al.* (1994) followed the method of Oppenheimer (1991) to extract thermal structures and radiative heat fluxes using TM data for active pahoehoe flows at Kilauea. This method was combined with an extended version of Pieri *et al.* (1990) to take into account saturation and non-response conditions, so that the dual-band method was applied as follows:

- A hot component temperature was assumed to achieve solution if bands 5 and 7 were unsaturated;
- In cases where the dual-band solution was not possible, and band 7 was unsaturated, the band 7 pixel-integrated temperature was used;
- Otherwise the band 5 pixel-integrated temperature was used, if band 5 was responsive.

The full execution of this procedure is detailed in Electronic Supplement 6. In addition, Flynn *et al.* (1994) used one band of unsaturated TIR (band 6) data to estimate skylight areas by applying the two-component, two-assumption model of Section 4.2.1.4 of Chapter 4. Its application, as executed by Flynn *et al.* (1994), is also detailed in Electronic Supplement 6.

(3) Andres and Rose (1995)

Andres and Rose (1995) provided dual-band-based estimates of the thermal structure over the active lava dome surface at Santiaguito using TM data and applying the approach of Rothery *et al.* (1998). However, response in band 4, as well as saturation of band 7, meant that Andres and Rose (1995) used bands 5 and 7, or bands 4 and 5 if band 7 was saturated and band 4 was responsive.

(4) Oppenheimer and Francis (1997)

Using TM data for Erta Ale, Oppenheimer and Francis (1997) worked further on tailoring solutions depending on the availability of saturated, useable, or non-responsive data in TM's SWIR and NIR bands (bands 4, 5 and 7). Accordingly, Oppenheimer and Francis (1997) set up the following five solution cases for pixels over the active lava lake:

(i) Case 1: Unsaturated data in band 7; no response in band 5
Solution: Assume hot component temperature and plot all possible combinations of crust temperature and pixel fraction which will give the band 7 pixel-integrated radiance.
[i.e., solution model (i) of Section 4.3.1.4., Chapter 4].

(ii) Case 2: Unsaturated data in bands 7 and 5
Solution: Apply the two-component dual-band solution by assuming a hot component temperature and solving for crust temperature and pixel fraction.
[i.e., solution model of Section 4.2.1.1, Chapter 4].

(iii) Case 3: Band 7 saturated; band 5 responsive and unsaturated
Solution: Assume hot component temperature and plot all possible combinations of crust temperature and pixel fraction which will give the band 5 pixel-integrated radiance.
[i.e., solution model (i) of Section 4.3.1.4., Chapter 4].

(iv) Case 4: Bands 5 and 7 saturated; band 4 responsive and unsaturated
Solution: Assume hot component temperature and plot all possible combinations of crust temperature and pixel fraction which will give the band 4 pixel-integrated radiance.
[i.e., solution model (i) of Section 4.3.1.4., Chapter 4].

(v) Case 5: Bands 5 and 7 saturated; no response in band 4
Solution: Use the minimum value required to generate response in band 4, assume a hot component temperature and plot all possible combinations of crust temperature and pixel fraction which will give this band 4 pixel-integrated temperature. Then narrow down the range to one that is plausible based on field constraints.
[i.e., solution model of Section 4.3.1.4. (see Figure 4.9), Chapter 4].

The fifth case is actually slightly modified over the Section 4.3.4 model, in that we have two bands of saturation and no-response in band 4, a case (unfortunately) that applied to most of Oppenheimer and Francis' (1997) pixels centered on the lake. In this case, the solution must lie above the solution line that defines all possible crust and fraction combinations that gives a DN of 255 in band 5, but below the solution line that defines all possible crust and fraction combinations to force a response on band 4.

(5) Oppenheimer (1998)

Oppenheimer (1998) applied the classic two-component approach to extract thermal structures and flow areas for carbonatite lava flows at Ol Doinyo Lengai using TM data. To do this, he took the Rothery *et al.* (1988) approach, assuming that hot flows were active against a non-radiant background in bands 5 and 7. However, instead of reaching a solution on a pixel-by-pixel basis, the band 5 and 7 radiances were summed over the entire anomaly (i.e., over all six anomalous pixels). This gave an anomaly-wide integrated spectral radiance of 0.36 mW cm^{-2} sr^{-1} μm^{-1} in band 5, and 1.56 mW cm^{-2} sr^{-1} μm^{-1} in band 7. Solution

(assuming an isothermal lava against an ambient background) then gave a flow area of 70 m^2 at a temperature of ~540 °C, values which are plausible for active carbonatite lavas at Ol Doinyo Lengai. This is effectively a hybrid of the, by now well established, unique one-component solution of Section 4.2.1.2 (Chapter 4), used with summed radiances obtained from the multiple-pixel-integration approach of Section 4.3.1.3 (Chapter 4). Note, though, that because all of the pixels were the same area and the anomaly was of the same size (and covered the same six pixels in both bands), the integrated radiance could be obtained from:

$$R_{\lambda\, int} = \sum_{i=1}^{n} (R_{\lambda i})$$

rather than the weighted average approach of Section 4.3.1.3.

(6) *Harris* et al. *(1999a)*

Harris *et al.* (1999a) began to explore three-component solutions using one band of TM data (i.e., the *One band of data, four assumptions* approach of Section 4.3.1.1 of Chapter 4). Also, following Oppeheimer and Francis (1998), Harris *et al.* (1999a) used saturated and non-responsive bands to help narrow down the range of possible solutions when only one band of unsaturated data were available (i.e., the Section 4.3.1.4. approach of Chapter 4).

The solution was for a case where a hot, two component body of known area (such as a lava lake or dome) was present against an ambient background, so that the pixel mixture model of Equation 4.17 (Chapter 4) could be applied

$$M(\lambda, T_{int}) = p_a\, M(\lambda, T_a) + p_c\, M(\lambda, T_c) + (1 - p_a - p_c)\, M(\lambda, T_h)$$

Given the hot feature area (A_{lava}), the pixel portion occupied by the hot feature (p_{lava}) could be calculated using the pixel area (A_{pixel}) in:

$$p_{lava} = A_{lava}/A_{pixel}$$

Thus, the area occupied by ambient ground (P_a) is:

$$p_a = 1 - p_{lava}$$

Fixing A_{lava} is particularly easy for a feature such as an active lava lake, because it is usually fairly easy to estimate the area, and the area usually stays approximately stable. This means that we have four unknowns, these being the temperature of the ambient background (T_a), the temperature of the crusted lava (T_c), the temperature of hot cracks in the active lava (T_h), and the pixel portion occupied by crust (p_c). This was reduced to two by assuming a temperature for T_h (~1000 °C) and setting T_a using the band 6 pixel-integrated temperatures for surrounding, hot spot free, pixels. Next, the band 6 pixel integrated temperature was used to plot all combinations of crust temperature and crust fraction that yielded the integrated value. Narrower constraint was obtained by using the output of each combination to calculate the pixel-integrated temperatures that would be expected in bands 4 and 5 (and/or 7). If there was saturation of band 5 and no response in band 4 then, once the band 4 result had increased to a level where detection would be expected, the solution could be rejected.

Likewise, if the band 5 result decreased to a level where the data were no longer saturated, then the solution could also be rejected.

(7) Lombardo and Buongiorno (2006)

The main post-2000 development was made by Lombardo and Buongiorno (2006), who took a slightly different approach to all previous studies, using a two-component model with three bands of data. All previous two-component models required at least one assumption, this usually being either for the temperature of the hot (crack) or cool (crust) component. The use of a two-component model, with three bands of data, allowed unconstrained solution with no assumptions. However, such a solution required use of airborne scanner data which provided three suitably located unsaturated bands. The scanner used was the Multispectral Infrared and Visible Imaging Spectrometer (MIVIS), which acquired data in 102 wavebands spanning the NIR, SWIR and TIR. Lombardo and Buongiorno (2006) used two unsaturated wavebands in the SWIR, and one in the TIR to achieve unconstrained solutions using data for the lava flow field active during Etna's July-August 2001 eruption.

Development of three-component and multiple component models

Most of these TM-based studies assumed that the pixel was filled by the hot active lava source, and applied a two-component model whereby the lava surface was composed of hot crust broken by even hotter cracks. Such a model could be solved easily using two wavebands of SWIR data. However, beginning in 1993, three-component models began to be developed which used three bands of data to allow inclusion of a third thermal component, or a consideration of the presence of lava-free surfaces at ambient temperature surrounding a two-component active lava feature. However, the approach was not developed that widely, being the subject of just two papers in the 1990s.

Oppenheimer (1993a)

Oppenheimer (1993a), using three bands of thermal data from an airborne scanner (the Thematic Mapper Simulator), was the first to consider a three-component solution. His solution considered a pixel filled by three thermal components: high temperature lava, cooler crusted lava, and low temperature active lava-free ground. Solution involved use of two wavebands of SWIR data [TMS bands 9 (1.55–1.75 μm, λ_{09}) and 10 (2.08–2.35 μm, λ_{10})] plus one band of TIR data [TMS band 11, 8.5–14.0 μm, λ_{11}]. For these bands, pixel-integrated radiances (in mW cm^{-2} sr^{-1} μm^{-1}) were respectively 0.290 (R_9), 0.624 (R_{10}) and 1.188 (R_{11}). This allowed three Equations to be constructed:

$$
\begin{aligned}
R_{11} &= p_h\, M(\lambda_{11}, T_h) + p_c\, M(\lambda_{11}, T_c) + (1 - p_h - p_c)\, M(\lambda_{11}, T_b) \\
R_{10} &= p_h\, M(\lambda_{10}, T_h) + p_c\, M(\lambda_{10}, T_c) + (1 - p_h - p_c)\, M(\lambda_{10}, T_b) \\
R_{09} &= p_h\, M(\lambda_{09}, T_h) + p_c\, M(\lambda_{09}, T_c) + (1 - p_h - p_c)\, M(\lambda_{09}, T_b)
\end{aligned}
$$

Two assumptions were made, that of:

(i) the background temperature (from surrounding lava-free TIR pixels) = 16 °C, and
(ii) the high temperature component (= 1075 °C).

Oppenheimer (1993a) then rearranged the band 11 equation and used this to get rid of p_c in the remaining two Equations. He then used these remaining two SWIR equations (based on the band 9 and 10 pixel-integrated radiances) to reach a solution. To do this Oppenheiner (1993) iterated on crust temperature (T_c) and pixel portion occupied by the high temperature component (p_h) until a solution was reached. His solution yielded T_c of 350 °C and p_h of 0.02 %. The crust component coverage (p_c) was then obtained by inputting the results into:

$$p_c = \frac{R_{11} - M(\lambda_{11}, T_a) - p_h[M(\lambda_{11}, T_h) - M(\lambda_{11}, T_a)]}{M(\lambda_{11}, T_c) - M(\lambda_{11}, T_a)}$$

that is,

$$p_c = \frac{3.37x10^7 Wm^{-2}m^{-1} - 2.52x10^7 Wm^{-2}m^{-1} - 0.0002[1.13x10^9 Wm^{-2}m^{-1} - 2.52x10^7 Wm^{-2}m^{-1}]}{3.06x10^8 Wm^{-2}m^{-1} - 2.52x10^7 Wm^{-2}m^{-1}}$$
$$= 0.042(4.2\%)$$

Although rearranged differently here, this is the methodology laid out in the *three bands, two assumptions* case of Chapter 4's Section 4.3.1.1.

Harris et al. (1999a)

Harris *et al.* (1999a) considered cases where the pixel may not be filled with active lava, as may occur at small (sub-pixel) features, such as active lava lakes in Landsat TM data. For such cases, a three-band model needs to be applied that considers a pixel containing an active lava surface comprising two thermal components (crust broken by hot cracks), surrounded by the third component – lava-free ground at ambient temperatures. Solution involved use of two wavebands of SWIR data [TM bands 5 (1.55 – 1.75 μm, λ_5) and 7 (2.08–2.35 μm, λ_7)] plus one band of TIR data [TM band 6, 10.4–12.5 μm, λ_6]. This allowed the *three bands of data, two assumptions* solution of Chapter 4's Section 4.3.1.1 to be applied, using the following system of Equations:

$$\begin{aligned} R_6 &= p_a\, M(\lambda_6, T_a) + p_h\, M(\lambda_6, T_h) + (1 - p_a - p_h)\, M(\lambda_6, T_c) \\ R_7 &= p_a\, M(\lambda_7, T_a) + p_h\, M(\lambda_7, T_h) + (1 - p_a - p_h)\, M(\lambda_7, T_c) \\ R_5 &= p_a\, M(\lambda_5, T_a) + p_h\, M(\lambda_5, T_h) + (1 - p_a - p_h)\, M(\lambda_5, T_c) \end{aligned}$$

The problem was, the TM band 6 pixel was larger than the band 5 and 7 pixels, being 120 m rather than 30 m and thus containing 16 smaller band 5 and 7 pixels. Harris *et al.* (1999a) thus followed the weighted-average approach of Section 4.3.1.3. (Chapter 4) to integrate the radiance for the smaller SWIR pixels across the larger TIR pixel to obtain an integrated value (R_{int}), i.e.,

$$R_{\lambda int} = \sum_{i=1}^{n} (\frac{1}{16} R_{\lambda i})$$

so that the system of Equations can be written,

$$\begin{aligned} R_6 &= p_a\, M(\lambda_6, T_a) + p_h\, M(\lambda_6, T_h) + (1 - p_a - p_h)\, M(\lambda_6, T_c) \\ R_{7int} &= p_a\, M(\lambda_7, T_a) + p_h\, M(\lambda_7, T_h) + (1 - p_a - p_h)\, M(\lambda_7, T_c) \\ R_{5int} &= p_a\, M(\lambda_5, T_a) + p_h\, M(\lambda_5, T_h) + (1 - p_a - p_h)\, M(\lambda_5, T_c) \end{aligned}$$

Harris *et al.* (1999a) chose to rearrange the first Equation in the series to isolate p_a, so that

$$p_a = \frac{R_6 - M(\lambda_6, T_a) - p_h[M(\lambda_6, T_h) - M(\lambda_6, T_c)]}{M(\lambda_6, T_a) - M(\lambda_6, T_c)} = \beta_6$$

Now inserting this into the second two Equations gives,

$$\begin{aligned} R_{7int} &= \beta_6\, M(\lambda_7, Ta_{)} + p_h\, M(\lambda_7, T_h) + (1 - \beta_6 - p_h)\, M(\lambda_7, T_c) \\ R_{5int} &= \beta_6\, M(\lambda_5, T_a) + p_h\, M(\lambda_5, T_h) + (1 - \beta_6 - p_h)\, M(\lambda_5, T_c) \end{aligned}$$

thereby getting rid of p_a. These two Equations were then solved by assuming a value for T_h and obtaining a value for T_a from ambient band 6 pixels surrounding the anomaly (in this case the lava lake), while ensuring that p_h, p_c and p_a were all positive and summed to one. Solution allowed the lava lake area to be estimated from:

$$A_{lake} = (p_h + p_c)\, A_{pixel}$$

In this case the pixel area (A_{pixel}) was that of the Landsat TM band 6 pixel (14 400 m^2) over which the band 5 and 7 spectral radiances were integrated. The problem was that there were not many cases where unsaturated, but anomalous, data were available in bands 5, 6 and 7; as a result Harris *et al.* (1999a) was only able to apply the solution to a single case: Erta Ale's Northern lava lake on a January 1986 image.

Harris et al. (2003)

Harris *et al.* (2003) later applied a similar three component approach to 29 TM and ETM+ images for Santiaguito's lava dome and silicic lava flows active between 1987 and 2000. The advantage here was that, given the relatively cool and heavily crusted nature of the lava flows they provided unsaturated data in three bands, although the extent of the flows themselves meant that the anomaly spread across multiple band 6 pixels, meaning that anomaly-wide integrated radiances were used. The full execution of this procedure is detailed in Electronic Supplement 6.

Application of the dual-band technique to AVHRR-class data

Beginning with Oppenheimer (1989), a set of studies began to consider the application of the dual band method to estimate lava area and surface temperature in lower spatial

resolution (1 km pixel) data. Oppenheimer (1989) applied the standard two-component model to unsaturated AVHRR data in a model that assumed the larger AVHRR-class pixel contained an isothermal high temperature (lava) surface against an ambient background. Oppenheimer (1989) expressed some reservations with this model, including the assumption of two thermal components, where the lava itself will likely comprise at least two components (cracks and crust). It was thus plain from the beginning that modifications would have to be made to the dual band method if it were to be applied to AVHRR data. For a start, AVHRR channel 3 (mid-infrared) data are often saturated over active lavas, so that only one band of TIR data can be used. As a result Harris *et al.* (1997a; 1997b) began to explore the potential of a two-component solution that uses one band of unsaturated TIR data to obtain lava area by assuming a temperature for the ambient background and a range of temperatures for the active lava surface. This, for Etna's 1991–1993 flow, gave reasonable results (see Figure 4.12 of Chapter 4) and allowed the surface leaving (radiative and convective) heat fluxes to be estimated. Wooster and Rothery (1997a) applied a similar approach to 1 km ATSR data, obtaining crust and crack (and hence total lava flow) areas by applying a two component model to the TIR and SWIR bands of ATSR, respectively. Like the AVHRR-based approach, this was initially applied to ATSR data for Etna's 1991–1993 lava flow (Wooster *et al.*, 1997), as well as to ATSR data for Fernandina's 1995 lava flow (Wooster and Rothery, 1997a), allowing estimation of the radiated heat flux.

Heat flux models

It was quickly realized that satellite TIR data were of great value in obtaining heat flux estimates for active volcanic phenomena, where the results of the dual-band method (surface temperature and area) are necessary inputs into heat flux calculation (see Section 4.4 of Chapter 4). The dual band method and heat flux estimations are thus natural companions. Table A2 of Appendix A shows that 50 of the 120 (42 %) satellite remote sensing papers published between 1965 and 2005 involved calculation of volcanic heat flux, with most of those publications also dealing with dual-band issues (i.e., covering theme areas 2 and 3 of Appendix A).

Active lava bodies

The first heat flux model using satellite data was applied by Friedman and Williams (1968). Using Nimbus HRIR data acquired during Surtsey's 1966 eruptions they calculated whole pixel radiative heat flux densities in ergs per second by using the pixel integrated temperature (T_{int}) in $\Phi_{rad} = \sigma T_{int}^4$. They then multiplied by pixel area (64 km^2) to obtain the radiative heat flux (M_{rad}) for Surtsey's pixel. Although not listed in the collation of Appendix A (because it was published as part of a conference proceedings), the results were soon published in the peer reviewed literature by Williams and Friedman (1970), as listed in Appendix A and reported in Chapter 1.

At the same time, as reviewed in Chapter 7, Decker and Peck (1967) used ground-based radiometers to estimate the surface leaving radiative energy flux for the cooling lava lake within Kilauea's Alae pit crater in 1964. However, it was not until the work of Glaze *et al.* (1989) that satellite data were again used to estimate heat fluxes over active lava bodies. In a Nature paper Glaze *et al.* (1989) showed how the dual-band method could be used with TM data to estimate the radiant heat flux for the lava dome at Lascar, as well as the lava lakes at Erebus and Erta Ale. They used the approach of Rothery *et al.* (1988) to estimate the temperature, and hence radiant flux density, of the radiating source, and then [like Friedman and Williams (1968)] multiplied by pixel area to obtain the radiation flux.

Pieri *et al.* (1990) moved towards a slightly more sophisticated approach that considered the contributions of both the hot cracks (at temperature T_h and occupying area A_h) and cooler crust (at T_c and occupying area A_c) to the radiative heat flux in:

$$M_{rad} = (\varepsilon \sigma T_h{}^4) A_h + (\varepsilon \sigma T_c{}^4) A_c$$

Applied to their dual-band solutions for a June 1984 TM scene of an active lava at Mount Etna, they were the first to use satellite (or radiometer) derived heat fluxes to estimate lava flow core cooling rates, their resulting map of core cooling being given in Figure 1.11 of Chapter 1.

While the study of Oppenheimer (1991) further refined the application of the dual-band method, it also provided a further improvement on heat loss estimates for lava flows and domes. For Lonquimay, Oppenheimer (1991) added an estimate of heat loss due to convection, as well as radiation, thereby moving towards a more complete heat budget for a lava flow. Oppenheimer (1991) also used Fourier's Law to apply the method of Section 4.4.1.4. of Chapter 4 to estimate crust thickness. His results are given in Figure 4.18 of Chapter 4. Other heat flux extractions, and their applications, at active lava flows, domes and lakes through the 1990s are summarized in Table S5.1.

Crater lakes, geothermal anomalies, open vents and fumaroles

Oppenheimer (1993b; 1996; 1997) focused on considering how TM data could be used to constrain the temperature and area of, plus heat flux from, crater lakes, with Gaonac'h *et al.* (1994) and Harris and Stevenson (1997) dealing with the measurement of heat fluxes at fumarole fields using TM data. However, heat loss inventories for geothermally heated surfaces and fumarole fields have tended to use radiometer-based surveys and/or thermal camera data, the subtle thermal anomalies associated with such features being easier to measure using a hand-held thermal camera placed at a suitable location close to the target. Hence, Matsushima *et al.* (2003) quickly adopted the thermal camera to apply the approach of Sekioka and Yuhara (1974) to obtain a heat flux inventory for Iwodake's fumarole field (see Section 4.4.1.12 of Chapter 4). We note here that the heat flux model of Sekioka and Yuhara (1974) for geothermal areas was originally designed to work with radiometer data, the use of a thermal camera allowing the measurements to be made across the entire surface,

rather than for selected points within it (see Chapter 7). The literature for volcanological applications of radiometers is given in Table 7.3 of Chapter 7, and for thermal cameras in Table 9.3 of Chapter 9. These show 15 radiometer-based inventories of fumarole fields and geothermal areas since 1965, and 12 thermal camera-based inventories since 2001, compared with just five satellite-based inventories (as collated in Table A2 of Appendix 2) – bearing out the fact that heat flux inventories for fumarole fields have not been the key role of satellite data, but are better suited to ground-based radiometry.

Conversion between lava flow heat flux and volume

The next level of conversion is to convert the dual-band extracted lava area and/or heat flux to lava volume or mass flux. Application of the first law of thermodynamics to estimate the heat budget of a lava flow on the basis of the mass or volume of the erupted lava can be traced to Verhoogen (1946) (see Section 4.5.1.1 of Chapter 4). A time line charting the post-1950 development and application of this approach to convert between lava mass (or volume) and heat flux is given in Figure S5.2. In this family tree, we see three generations of study:

- Generation 1: Studies up until 1980 tended to use measurements of lava volume or mass to estimate the heat liberated by the lava mass in cooling to ambient. Yokoyama (1957) was one of the first to do this, followed by Williams and Friedman (1970) and Scandone (1979).
- Generation 2: Beginning with Pieri and Baloga's (1986) exploration of the relation between lava discharge rate and lava flow area, studies began to convert the other way: between heat flux and mass or volume. In fact, Pieri and Baloga's (1986) study became extremely influential in guiding attempts to convert satellite-derived heat flux, or lava flow area, to lava discharge rate (TADR), i.e., the rate at which lava needs to be supplied to maintain the active lava area. From the Figure S5.2 time line we see that, after this publication, an increasing number of studies attempted to use IR data to execute conversions between heat flux, or lava flow area, and TADR, mass or volume. These studies are collated in Table S5.2.
- Generation 3: Studies that helped to refine the technique, as well as to clarify its application limits and assumptions. These advances were made in parallel with continued application to convert (mostly satellite) IR data to TADR for a variety of eruptions using a range of sensors (see Table S5.2).

Although the volume-to-heat flux conversion of Friedman and Williams (1968) and Williams and Friedman (1970) appeared in papers which used satellite data to examine an eruption related hot spot, they did not use the satellite data in making the conversion. Instead they used field-measured volume flux to estimate the amount of energy they expected from the volcanic source, and compared that with the energy recorded for a 64 km^2 NIMBUS II pixel centered on Surtsey. Le Guern (1987) was probably the first attempt to use an IR (in his case radiometer-based) measurement to obtain a heat flux, and then convert the heat flux to a

Table S5.2. *Application and development of the thermal approach to extract lava discharge rates, showing the range of eruption scenarios to which the conversion has been applied and data types used. Acronyms used are: AVHRR (Advanced Very High Resolution Radiometer), ATSR (Along Track Scanning Radiometer), TM (Thematic Mapper), ETM+ (Enhanced Thematic Mapper Plus) and FLIR (Forward Looking Infrared Radiometer). Modified from Table 1 of Harris* et al. *(2007).*

Volcano	Eruption/Years	Eruption Type / Effusive or Extrusive Style	Data	Reference
Bezymianny	2000	Lava dome	AVHRR, MODIS	Steffke (2005)
Erebus	1985 & 1989	Lava lake	TM	Harris *et al.* (1999a)
Erebus	1980	Lava lake	AVHRR	Harris *et al.* (1999b)
Erta Ale	1986	Lava lake	TM	Harris *et al.* (1999a)
Etna	1991–1993	Flank eruption (channel & tube fed 'a'a)	AVHRR	Harris *et al.* (1997a)
Etna	1980–1999[a]	Flank & summit eruptions (channel & tube fed 'a'a)	AVHRR, ATSR, TM	Harris *et al.* (2000)
Etna	November 1999	Fountain-fed (channel fed 'a'a) lava flows	AVHRR, ETM+	Harris & Neri (2002)
Etna	2001[b]	Summit & flank eruption (channel & tube fed 'a'a)	AVHRR	Lautze *et al.* (2004)
Fernandina	1995	Flank eruption (channel fed 'a'a)	ATSR	Rowland *et al.* (2003)
Kilauea	1991	Tube-fed pahoehoe	AVHRR & TM	Harris *et al.* (1998)
Kilauea	1991	Lava lake (Pu'u 'O'o)	TM	Harris *et al.* (1999a)
Krafla	1980–1984[c]	Fissure eruptions (fountain & channel fed 'a'a)	AVHRR	Harris *et al.* (2000)
Mt. Cleveland	2001	'A'a lava flow	AVHRR	Smith (2005)
Nyiragongo	1987	Lava lake	TM	Harris *et al.* (1999a)
Okmok	1997	'A'a lava flow (some of it ponded)	AVHRR	Patrick *et al.* (2003)
Santiaguito	1987–2000	Dome & silicic lava flow extrusion	TM & ETM+	Harris *et al.* (2003)
Santiaguito	2000	Silicic lava flow extrusion	ETM+	Harris *et al.* (2002)
Santiaguito	2000–2002	Silicic lava flow extrusion	TM & ETM+	Harris *et al.* (2004)
Stromboli	1985–1986	Flank eruption (channel & tube fed 'a'a)	AVHRR	Harris *et al.* (2000)
Stromboli	2002–2003	Flank eruption (channel & tube fed 'a'a)	AVHRR, MODIS	Calvari *et al.* (2005)
Stromboli	2002–2003	Flank eruption (channel & tube fed 'a'a)	FLIR	Harris *et al.* (2005)

[a] March 1981, February 1981, 1983, 1984, March-July 1985, December 1985, 1986–87, September 1989, September – October 1989, 1991–1993, 1996, and 1999 eruptions.

[b] January – July SE Crater eruption and July – August S. Flank eruption.

[c] July 1980, October 1980, January – February 1981, and 1984 eruptions.

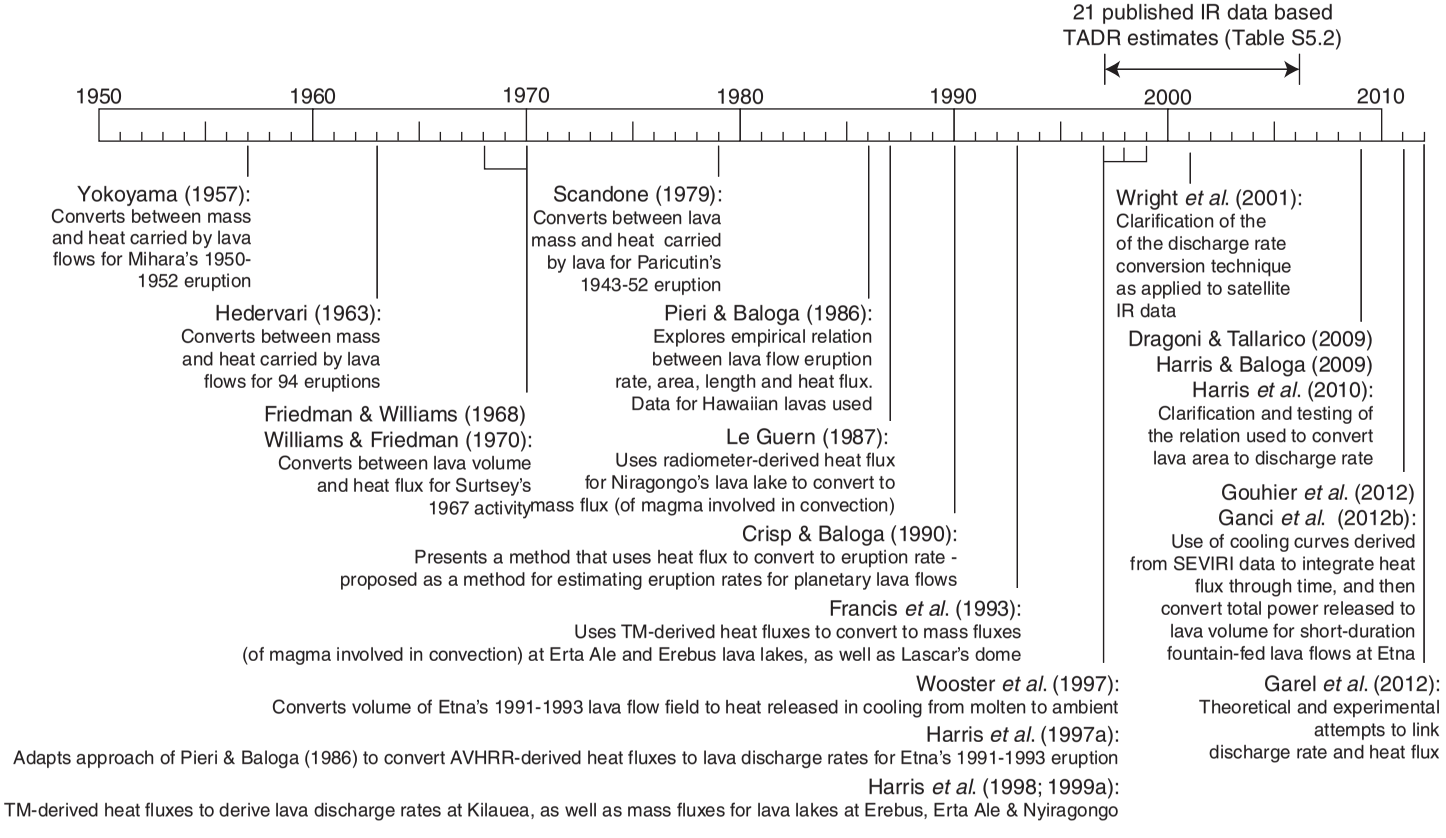

Figure S5.2 Time line for studies involving conversion of heat flux to lava mass or volume (or vice versa), with a special emphasis on use of thermal sensors to estimate time-averaged discharge rate and lava volume.

mass flux of lava required to generate the observed heat flux, with Francis *et al.* (1993) using TM-derived heat fluxes to achieve the same conversion for a number of active lava lakes and domes. Coupled with these two studies, Crisp and Baloga (1990), in an *Icarus* paper, suggested the relation between heat flux and volume flux could be used for extra-terrestrial applications. Harris *et al.* (1997a) then tested the relation of Pieri and Baloga (1986) with terrestrial data for an active lava flow. This initial test used AVHRR data for Etna's 1991–1993 eruption and yielded promising results. Between 1997 and 2006, 21 studies tested and applied methods to estimate discharge rates at lava lakes, domes, basaltic and silicic lava flows using a range of satellite data sets, including AVHRR, ATSR, MODIS, TM, ETM+ and ASTER, as well as hand-held thermal camera (FLIR) data (see Table S5.2). The time line of Figure S5.2 flags those post-1997 studies that have attempted to further modify and clarify the conversion routine. These studies have pointed to the fact that, when applied using a two-component TIR mixture model as its basis, the satellite data-based conversion reduces to a linear relation between TADR and lava area (Wright *et al.*, 2001). This relation has to be set and checked (using ground truth data, i.e., a field-based measure of TADR) on a case-by-case basis (Harris and Baloga, 2009), as described in the of later sections of Chapter 4.

More recently, studies have used satellite-derived discharge rates to run lava flow emplacement simulations. Wright *et al.* (2008) used a combination of the FLOWGO and DOWNFLOW lava flow emplacement models, with AVHRR-derived discharge rates, to simulate emplacement of Etna's 1991–1993 lava flow field. Comparisons between maps generated by the satellite data-driven simulations and actual (field-mapped) flow areas are given in Figure S5.3. These show that, when supplied with satellite-derived discharge rates, realistic assessments of lava flow inundation and run-out (or length) can be achieved. Instead, Herault *et al.* (2009) and Vicari *et al.* (2009; 2011) used the MAGFLOW cellular automata model, with MODIS-derived discharge rates, to simulate Etna's July 2006 lava flow, as well as fountain fed lava flow during Etna's 12–13 January 2011 eruption. Simulated flow inundation areas were, again, in good agreement with field-based maps. The result has been efforts to generate integrated real-time monitoring and response systems, such as the LAV@HAZARD system of Ganci *et al.* (2012a). As reviewed in Chapter 5, the aims of such systems are to ingest satellite data in real-time and execute automated algorithms to (i) detect the hot spot, (ii) execute a thermal mixture model, (iii) convert to heat flux and discharge rate, and (iv) execute a lava flow simulation.

Three recent studies have used SEVIRI data to identity cooling curves following short, fountain-fed lava flow emplacement events (Calvari *et al.*, 2011; Gouhier *et al.*, 2012; Ganci *et al.*, 2012b). Integrating the heat flux through time allows total power during cooling to be estimated, which (following methodologies laid out in Section 5 of Chapter 4) can be converted to a total lava volume. The result allows rapid generation of lava volumes erupted during fountaining events, with Ganci *et al.*'s (2012b) SEVIRI-derived inventory of all lava fountain events on Etna between January 2011 and January 2012 being given, by way of example, in Table S5.3.

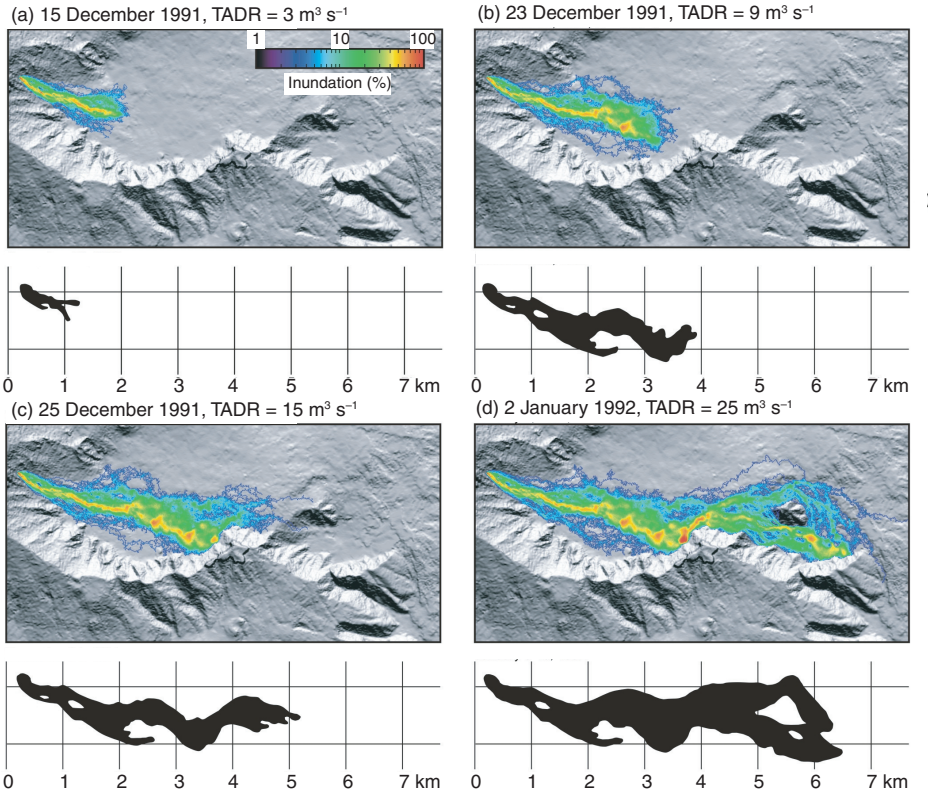

Figure S5.3 FLOWGO/DOWNFLOW simulations using TADRs determined from AVHRR data acquired during the first 19 days of Etna's 1991–1993 eruption, with published maps of flow dimensions. DOWNFLOW projects a flow line (line of steepest descent) multiple times from the user-selected source (vent) to the edge of the Digital Elevation Model (DEM). Random noise is added to the DEM between each run so that a slightly different flow line is obtained during each iteration (Favalli *et al.*, 2005). FLOWGO then estimates the cooling-limited distance that lava can travel down each line at a given TADR (Harris and Rowland, 2001). In this case, the model was run 5000 times for each simulation, using the AVHRR-derived TADR obtained by Harris *et al.* (1997) for each simulation day. Sketch maps of the flow extent around the same time as each model run are taken from Calvari and Pinkerton (1998) and given below each simulation. Images and sketches are displayed at the same horizontal and vertical scale to allow direct comparison. The color on the simulations denotes the number of times a pixel has been used by a flow line, and is labeled "inundation". The model provides a good approximation of field-mapped flow length and area, and the inundation assessment appears a good proxy for final flow thickness [From Wright *et al.* (2008, Fig. 3): Reproduced by permission of American Geophysical Union].

Summation

Given that the literature data base given in this book consists 120 papers that use satellite data for volcano hot spot radiometry (Appendix A), 67 papers that use radiometer data (Table 7.3 of Chapter 7), and 113 papers that explore thermal camera applications (Table 9.3

Table S5.3. *SEVIRI-derived lava flow volumes from cooling-curve methodology of Chapter 4 (Section 5), for short (<14 hour long) lava fountain events on Etna [From Tables 1 and 2 of Ganci* et al. *(2012b)]. Cooling curves are fitted to SERVIRI-derived heat flux data following each lava fountain event. These are used to obtain the lava volume required to generate the observed decay in heat flux. Between January 2011 and January 2012 there were 19 lava fountain events, of which 18 were detected by SEVIRI. However, seven events suffered from cloud and ash contamination problems (indicated by use of gray background). Output rate is total volume divided by total duration.*

Lava Fountain Date	Detected By SEVIRI?	Weather Conditions	Ash Interference	Cooling Curve	Volume [m^3]	Duration [minutes]	Mean Output Rate [$m^3\ s^{-1}$]
January 12–13, 2011	YES	Clear Sky	During Fountaining	YES	1550000	255	101.2
February 18, 2011	NO	Covered	Cloud covered	NO	N/A	N/A	N/A
April 10, 2011	YES	Clear Sky	During & after Fountaining	YES	877000	495	29.5
May 11–12, 2011	YES	Clear Sky	During Fountaining	YES	1474000	570	43.1
July 9, 2011	YES	Clear Sky	During Fountaining	YES	1492000	243	102.3
July 18–19, 2011	YES	Clear Sky	Minor	YES	2139000	240	148.5
July 24–25, 2011	YES	Cloudy	Minor	YES	988000	630	26.1
July 30–31, 2011	YES	Partly Cloudy	Minor	YES	2223000	810	45.7
August 5–6, 2011	YES	Clear Sky	Minor	YES	1588000	270	98.0
August 12, 2011	YES	Clear Sky	Minor	YES	2857000	210	226.7
August 20, 2011	YES	Slightly Cloudy	During & after Fountaining	YES	1401000	330	70.8
August 29, 2011	YES	Slightly Cloudy	During Fountaining	YES	1739000	255	113.7
September 8, 2011	YES	Slightly Cloudy	During Fountaining	YES	1216000	180	112.6
September 19, 2011	YES	Almost Covered	Cloud covered	NO	N/A	N/A	N/A
September 28–29, 2011	YES	Cloudy	Minor	YES	406000	228	29.7
October 8, 2011	YES	Cloudy	Minor	YES	843000	465	30.2
October 23–24, 2011	YES	Almost Clear Sky	Minor	YES	1311000	150	145.7
November 15, 2011	YES	Slightly Cloudy	Minor	YES	1809000	273	110.4
January 5, 2012	YES	Slightly Cloudy	During Fountaining	YES	1494000	318	78.3

of Chapter 9), writing a history of every element of radiometry-based methodologies and applications presents a mammoth task. Here I have tried to complete a thorough history of the dual-band method, added to which is a short review of its application to extract heat and volume fluxes. More detailed histories are given within this book for:

- The development of IR sensors and their application in volcano radiometry (Chapter 1);
- The extraction of heat and mass fluxes for active volcanic phenomena (Chapter 4);
- Hot spot detection in, and time series generation from, satellite data for volcanic (and fire-related) hot spots (Chapters 5 and 6, plus the associated supplements);
- The use of radiometers and thermal cameras in volcanology (Chapters 7 and 9).

I hope that any researcher wanting to complete a background review of any theme in volcano radiometry can use the literature data bases given in this book to obtain a complete history of any desired theme or theme combinations, many of which I am bound to have missed. General theme areas that these literature data bases support are:

(i) Sensor or data types used in volcano radiometry (spanning satellite and ground-based sensors),
(ii) Applications by thermal anomaly type (lava flow, dome, geothermal, etc),
(iii) Development of data processing and reduction methodologies, and IR data applications for measuring and tracking thermal phenomena,

Plus any combination of data type, target type, methodology or application.

References

Abrams, M., Glaze, L. and Sheridan, M. (1991). Monitoring Colima volcano, Mexico, using satellite data. *Bulletin of Volcanology*, **53**, 571–574.

Andres, R. J. and Rose, W. I. (1995). Description of thermal anomalies on two active Guatemalan volcanoes using Landsat Thematic Mapper Imagery. *Photogrammetric Engineering and Remote Sensing*, **61**(6), 775–782.

Bhattacharya, A., Reddy, C. S. S. and Srivastav, S. K. (1993). Remote sensing for active volcano monitoring. *Photogrammetric Engineering and Remote Sensing*, **59**(8), 1293–1297.

Calvari, S. and Pinkerton, H. (1998). Formation of lava tubes and extensive flow field during the 1991–93 eruption of Mount Etna. *Journal of Geophysical Research*, **103**, 27291–27302.

Calvari, S., Spampinato, L., Lodato, L., Harris, A. J. L., Patrick, M. R., Dehn, J., Burton, M. R. and Andronico, D. (2005). Chronology and complex volcanic processes during the 2002–2003 flank eruption at Stromboli volcano (Italy) reconstructed from direct observations and surveys with a handheld thermal camera. *Journal of Geophysical Research*, **110**, B02201. DOI: 10.1029/2004JB003129

Calvari, S., Salerno, G. G., Spampinato, L., Gouhier, M., La Spina, A., Pecora, E., Harris, A. J. L., Labazuy, P., Biale, E. and Boschi, E. (2011). An unloading foam model to constrain Etna's 11–13 January 2011 lava fountaining episode. *Journal of Geophysical Research*, **116**, B11207, DOI: 10.1029/2011JB008407.

Crisp, J. and Baloga, S. (1990). A method for estimating eruption rates of Planetary lava flows. *Icarus*, **85**(2), 512–515.

Decker, R. W. and Peck, D. L. (1967), Infrared radiation from Alae lava lake, Hawaii. *U.S. Geological Survey Professional Paper*, **575-D**, D169–D175.

Dozier, J. (1980). Satellite identification of surface radiant temperature fields of subpixel resolution. *NOAA Technical Memorandum*, **NOAA-81021710**, Washington DC: National Earth Satellite Service, 17 p.

Dozier, J. (1981). A method for satellite identification of surface temperature fields of subpixel resolution. *Remote Sensing of Environment*, **11**, 221–229.

Dragoni, M. and Tallarico, A. (2009). Assumptions in the evaluation of lava effusion rates from heat radiation. *Geophysical Research Letters*, **36**, L08302. DOI: 10.1029/2009GL037411.

Favalli, M., Pareschi, M. T., Neri, A. and Isola, I. (2005). Forecasting lava flow paths by a stochastic approach. *Geophysical Research Letters*,, **32**, L03305. DOI: 10.1029/2004GL021718.

Flynn, L. P., Mouginis-Mark, P. J. and Horton, K. A. (1994). Distribution of thermal areas on an active lava flow field: Landsat observations of Kilauea, Hawaii, July 1991. *Bulletin of Volcanology*, **56**, 284–296.

Francis, P. W. and Rothery, D. A. (1987). Using the Landsat Thematic Mapper to detect and monitor active volcanoes: An example from Lascar volcano, northern Chile. *Geology*, **15**, 614–617.

Francis, P., Oppenheimer, C. and Stevenson, D. (1993). Endogenous growth of persistently active volcanoes. *Nature*, **366**, 554–557.

Friedman, J. D. and Williams, R. S. (1968). Infrared sensing of active geologic features. *Proceedings of the 5th Symposium on Remote Sensing of Environment*. Ann Arbor (Michigan): University of Michigan Institute of Science and Technology, pp. 787–820.

Ganci, G., Vicari, A., Cappello, A. and Del Negro, C. (2012a). An emergent strategy for volcano hazard assessment: From thermal satellite monitoring to lava flow modeling. *Remote Sensing of Environment*, **119**, 197–207.

Ganci, G., Harris, A. J. L., Del Negro, C., Guehenneux, Y., Cappello, A., Labazuy, P., Calvari, S. and Gouhier, M. (2012b). A year of lava fountaining at Etna: Volumes from SEVIRI. *Geophysical Research Letters*, **39**, L06305. DOI: 10.1029/2012GL051026.

Garel, F., Kaminski, E., Tait, S. and Limare, A. (2012). An experimental study of the surface thermal signature of hot subaerial isoviscous gravity currents: Implications for thermal monitoring of lava flows and domes. *Journal of Geophysical Research*, **117**, B02205. DOI: 10.1029/2011JB008698.

Gaonac'h, H., Vandemeulebrouck, J., Stix, J. and Halbwachs, M. (1994). Thermal infrared satellite measurements of volcanic activity at Stromboli and Vulcano. *Journal of Geophysical Research*, **99**(B5), 9477–9485.

Glaze, L., Francis, P. W. and Rothery, D. A. (1989). Measuring thermal budgets of active volcanoes by satellite remote sensing. *Nature*, **338**, 144–146.

Gouhier, M., Harris, A., Calvari, S., Labazuy, P., Guéhenneux, Y., Donnadieu, F. and Valade, S. (2012). Lava discharge during Etna's January 2011 fire fountain tracked using MSG-SEVIRI. *Bulletin of Volcanology*. DOI: 10.1007/s00445-011-0572-y

Gupta, R. K. and Badarinath, K. V. S. (1993). Volcano monitoring using remote sensing data. *International Journal of Remote Sensing*, **14**(16), 2907–2918.

Harris, A. J. L. and Neri, M. (2002). Volumetric observations during paroxysmal eruptions at Mount Etna: pressurized drainage of a shallow chamber or pulsed supply? *Journal of Volcanology and Geothermal Research*., **116**, 79–95.

Harris, A. J. L. and Baloga, S. M. (2009). Lava discharge rates from satellite-measured heat flux. *Geophysical Research. Letters*, **36**, L19302. DOI: 10.1029/2009GL039717

Harris, A. J. L. and Rowland, S. K. (2001). FLOWGO: a kinematic thermo–rheological mode for lava flowing in a channel. *Bulletin of Volcanology*, **63**, 20–44.

Harris, A. J. L. and Stevenson, D. S. (1997). Thermal observations of degassing open conduits and fumaroles at Stromboli and Vulcano using remotely sensed data. *Journal of Volcanology and Geothermal Research.*, **76**, 175–198.

Harris, A. J. L., Blake, S., Rothery, D. A. and Stevens, N. F. (1997a). A chronology of the 1991 to 1993 Etna eruption using AVHRR data: implications for real time thermal volcano monitoring. *Journal of Geophysical Research*, **102**(B4), 7985–8003.

Harris, A. J. L., Butterworth, A. L., Carlton, R. W., Downey, I., Miller, P., Navarro, P. and Rothery, D. A. (1997b). Low cost volcano surveillance from space: case studies from Etna, Krafla, Cerro Negro, Fogo, Lascar and Erebus. *Bulletin of Volcanology*, **59**, 49–64.

Harris, A. J. L., Flynn, L. P., Keszthelyi, L., Mouginis-Mark, P. J., Rowland, S. K. and Resing, J. A. (1998). Calculation of Lava Effusion Rates from Landsat TM Data. *Bulletin of Volcanoogy*, **60**, 52–71.

Harris, A. J. L., Flynn, L. P., Rothery, D. A., Oppenheimer, C. and Sherman, S. B. (1999a) Mass flux measurements at active lava lakes: implications for magma recycling. *Journal of Geophysical Research*, **104**, 7117–7136.

Harris, A. J. L., Wright, R. and Flynn, L. P. (1999b). Remote monitoring of Mount Erebus Volcano, Antarctica, using Polar Orbiters: Progress and Prospects. *Internal Journal of Remote Sensing*, **20**(15&16), 3051–3071.

Harris, A. J. L., Murray, J. B., Aries, S. E., Davies, M. A., Flynn, L. P., Wooster, M. J., Wright, R. and Rothery, D. A. (2000). Effusion rate trends at Etna and Krafla and their implications for eruptive mechanisms. *Journal of Volcanology and Geothermal Research*, **102**, 237–270.

Harris, A. J. L., Flynn, L. P., Matías, O. and Rose, W. I. (2002). The thermal stealth flows of Santiaguito: implications for the cooling and emplacement of dacitic block lava flows. *Geological Society of America Bulletin*, **114**, 533–546.

Harris, A. J. L., Flynn, L. P. and Rose, W. I. (2003). Temporal trends in Lava Dome Extrusion at Santiaguito 1922–2000. *Bulletin of Volcanology*, **65**, 77–89.

Harris, A. J. L., Flynn, L. P., Matias, O., Rose, W. I. and Cornejo, J. (2004). The evolution of an active silicic lava flow field: An ETM+ perspective. *Journal of Volcanology and Geothermal Research*, **135**, 147–168.

Harris, A. J. L., Dehn, J., Patrick, M., Calvari, S., Ripepe, M. and Lodato, L. (2005). Lava Effusion Rates from Hand-Held Thermal Infrared Imagery: An Example from the June 2003 Effusive Activity at Stromboli. *Bulletin of Volcanology*, **68**, 107–117.

Herault, A., Vicari, A., Ciraudo, A. and Del Negro, C. (2009). Forcasting lava flow hazards during the 2006 Etna eruption: Usging the MAGFLOW cellular automata model. *Computers & Geosciences*, **35**, 1050–1060.

Hérdervári, P. (1963). On the energy and magnitude of volcanic eruptions. *Bulletin of Volcanology*, **25**, 373–385.

Lautze, N. C., Harris, A. J. L., Bailey, J. E., Ripepe, M., Calvari, S., Dehn, J., Rowland, S. and Evans-Jones, K. (2004). Pulsed lava effusion at Mount Etna during 2001. *Journal of Volcanology and Geothermal Research*, **137**, 231–246.

Le Guern, F. (1987). Mechanism of energy transfer in the lava lake of Niragongo (Zaire), 1959–1977. *Journal of Volcanology and Geothermal Research*, **31**, 17–31.

Lombardo, V. and Buongiorno, M. F. (2006) Lava flow thermal analysis using three infrared bands of remote-sensing imagery: A study case from Mount Etna 2001 eruption. *Remote Sensing of Environment*, **101**, 141–149.

Matson, M. and Dozier, J. (1981). Identification of subresolution high temperature sources using a thermal IR sensor. *Photogrammetric Engineering and Remote Sensing*, **47**(9), 1311–1318.

Matsushima, N., Kazahaya, K., Saito, G. and Shinohara, H. (2003). Mass and heat flux of volcanic gas discharging from the summit crater of Iwodake volcano, Satsuma-Iwojima, Japan, during 1996–1999. *Journal of Volcanology and Geothermal Research*, **126**, 285–301.

Oppenheimer, C. (1989). AVHRR volcano hot spot monitoring. *Proceedings of the 4th AVHRR data users' meeting*. Rothenberg (Sweden): 3–5 September 1989, pp. 335–338.

Oppenheimer, C. (1991). Lava flow cooling estimated from Landsat Thematic Mapper infrared data: the Lonquimay eruption (Chile, 1989). *Journal of Geophysical Research*, **96**(B13), 21865–21878.

Oppenheimer, C. (1993a). Thermal distributions of hot volcanic surfaces constrained using three infrared bands of remote sensing data. *Geophysical Research Letters*, **20**(6), 431–434.

Oppenheimer, C. (1993b). Infrared surveillance of crater lakes using satellite data. *Journal of Volcanology and Geothermal Research*, **55**, 117–128.

Oppenheimer, C. (1996). Crater lake heat losses estimated by remote sensing. *Geophysical Research Letters*, **23**(14), 1793–1796.

Oppenheimer, C. (1997). Remote sensing of the colour and temperature of volcanic lakes. *International Journal of Remote Sensing*, **18**(1), 5–37.

Oppenheimer, C. (1998). Satellite observation of active carbonatite volcanism at Ol Doinyo Lengai, Tanzania. *International Journal of Remote Sensing*, **19**(1), 55–64.

Oppenheimer, C. and Francis, P. (1997). Remote sensing of heat, lava and fumarole emissions from Erta 'Ale volcano, Ethiopia. *International Journal of Remote Sensing*, **18**(8), 1661–1692.

Oppenheimer, C., Francis, P. W., Rothery, D. A., Carlton, R. W. T. and Glaze, L. S. (1993). Infrared image analysis of volcanic thermal features: Lascar Volcano, Chile. *Journal of Geophysical Research*, **98**(B3), 4269–4286.

Patrick, M. R., Dehn, J., Papp, K. R., Lu, Z., Dean, K., Moxey, L., Izbekov, P. and Guritz, R. (2003). The 1997 eruption of Okmok Volcano, Alaska: a synthesis of remotely sensed imagery. *Journal of Volcanology and Geothermal Research*, **127**, 87–105.

Pieri, D. C. and Baloga, S. M. (1986). Eruption rate area, and length relationships for some Hawaiian lava flows. *Journal of Volcanology and Geothermal Research*, **30**, 29–45.

Pieri, D. C., Glaze, L. S. and Abrams, M. J. (1990). Thermal radiance observations of an active lava flow during the June 1984 eruption of Mount Etna. *Geology*, **18**, 1018–1022.

Reddy, C. S. S., Bhattacharya, A. and Srivastav, S. K. (1993). Night-time TM short wavelength infrared data analysis of Barren Island volcano, South Andaman, India. *International Journal of Remote Sensing*, **14**(4), 783–787.

Rothery, D. A., Francis, P. W. and Wood, C. A. (1988). Volcano monitoring using short wavelength infrared data from satellites. *Journal of Geophysical Research*, **93**(B7), 7993–8008.

Rowland, S. K., Harris, A. J. L., Wooster, M. J., Amelung, F., Garbeil, H., Wilson, L. and Mouginis-Mark, P. J. (2003). Volumetric Characteristics of Lava Flows from Interferometric Radar and Multispectral Satellite Data. *Bulletin of Volcanology*, **65**, 311–330.

Scandone, R. (1979). Effusion rate and energy balance of Paricutin eruption (1943–1952), Michoacan, Mexico. *Journal of Volcanology and Geothermal Research*, **6**, 49–59.

Sekioka, M. and Yuhara, K. (1974). Heat flux estimation in geothermal areas based on the heat balance of the ground surface. *Journal of Geophysical Research*, **79**(14), 2053–2058.

Steffke, A. M. (2005). Temperatures, Thermal Fluxes and Effusion Rates Associated with the Growth of Bezymianny Volcano using Spaceborne Thermal Infrared Data. MS Thesis, University of Alaska, Fairbanks.

Smith, S. J. (2005). Chronologic Multisensor Assessment for Mount Cleveland, Alaska from 2000 to 2004 focusing on the 2001 eruption. MS Thesis, University of Alaska Fairbanks.

Verhoogen, J. (1946). Volcanic heat. *American Journal of Science*, **244**(11), 745–771.

Vicari, A., Ciraudo, A., Del Negro, C., Herault, A. and Fortuna, L. (2009). Lava flow simultations using discharge rates from thermal infrared satellite imagery during the 2006 Etna eruption. *Natural Hazards*, **50**, 539–550.

Vicari, A., Ganci, G., Behncke, B., Cappello, A., Neri, M. and Del Negro, C. (2011). Near-real-time forecasting of lava flow hazards during the 12–13 January 2011 Etna eruption. *Geophysical Research Letters*, **38**, L13317. DOI: 10.1029/2011GL047545.

Williams, R. S. and Friedman, J. D. (1970). Satellite observation of effusive volcanism. *Journal of the British Interplanetary Society*, **23**, 441–450.

Wooster, M. J. and Rothery, D. A. (1997a). Time-series analysis of effusive volcanic activity using the ERS Along Track Scanning Radiometer: The 1995 eruption of Fernandina Volcano, Galápagos Islands. *Remote Sensing of Environment*, **62**, 109–117.

Wooster, M. J. and Rothery, D. A. (1997b). Thermal monitoring of Lascar Volcano, Chile, using infrared data from the along-track scanning radiometer: a 1992–1995 time series. *Bulletin of Volcanology*, **58**, 566–579.

Wooster, M. J., Wright, R., Blake, S. and Rothery, D. A. (1997). Cooling mechanisms and an approximate thermal budget for the 1991–1993 Mount Etna lava flow. *Geophysical Research Letters*, **24**(24), 3277–3280.

Wright, R., Blake, S., Harris, A. and Rothery, D. (2001). A simple explanation for the space-based calculation of lava eruptions rates. *Earth and Planetary Science Letters*, **192**, 223–233.

Wright, R., Garbeil, H. and Harris, A. J. L. (2008). Using infrared satellite data to drive a thermo-rheological/stochastic lava flow emplacement model: A method for near-real-time volcanic hazard assessment. *Geophysical Research Letters*, **35**, L19307,. DOI: 10.1029/2008GL035228.

Yokoyama, I. (1957). Energetics in active volcanoes. 2nd Paper. *Bulletin of the Earthquake Research Institute*, **35**, 75–97.